MAGNETIC
RESONANCE
Discussions

Dynamic view of the solid-state DNP effect

Deniz Sezer

Institute of Physical and Theoretical Chemistry, Goethe University, 60438 Frankfurt am Main, Germany

Correspondence: Deniz Sezer (dzsezer@gmail.com)

Abstract. The first report of dynamic nuclear polarization (DNP) in liquids via the solid-effect mechanism [Erb, Motchane and Uebersfeld *Compt. rend.* **246**, 2121 (1958)] drew attention to the similarity between the field profile of the enhancement and the dispersive component of the EPR line. The implications of this similarity, however, were not pursued subsequently as practically at the same time Abragam explained the effect in terms of state mixing by the dipolar interaction. Here we develop a description of the solid effect which is grounded in the dynamics of the electron-nucleus spin system, rather than the static view of state mixing. Our approach highlights the role of the coherences in the polarization transfer, and shows that the offset dependence of the DNP enhancement can be rationalized as the response of two band-pass filters connected in series. The first filter is the power-broadened EPR line; the second filter consists of two parts centered on both sides of the electronic resonance and displaced by one nuclear Larmor frequency from it. Being proportional to the product of the two filters, the DNP enhancement profile acquires its odd symmetry from the dispersive EPR line, as intuited by Erb et al. and in agreement with their phenomenological treatment. The developed time-domain description of the solid effect is extendable to liquids where the dipolar interaction changes randomly in time due to molecular diffusion.

1 Introduction

The issue of *Comptes rendus* from April 9, 1958, contained the article "Effect of nuclear polarization in liquids and gases adsorbed on charcoal" by Erb, Motchane and Uebersfeld (Erb et al., 1958a). It reported enhancements of the proton NMR signal of benzene upon microwave (mw) irradiation of the EPR line of charcoal. The enhancements were positive at fields larger than the EPR resonance position and negative at smaller fields. Because fields symmetrically displaced from the resonance yielded the same magnification factor, the enhancement profile was odd in the field offset and resembled the dispersive component of the EPR line. The similarity between the two prompted the authors to augment the Solomon equation (Solomon, 1955) with two new terms proportional to s_x and s_y (Erb et al., 1958a):

$$\dot{i}_z = \lambda(i_z - i_z^{\mathrm{eq}}) + \mu(s_z - s_z^{\mathrm{eq}}) + \nu s_x + \rho s_y. \tag{1}$$

Here $i_z = \langle I_z \rangle$ and $s_n = \langle S_n \rangle$ $(n = x, y, z)$ are the expectation values of the corresponding spin operators, i_z^{eq} and s_z^{eq} are the nuclear and electronic polarizations at equilibrium, and the dot above i_z indicates differentiation with respect to time. Taking into account that "under saturation conditions $s_y = 0$" the authors arrived at

$$\dot{i}_z = \lambda(i_z - i_z^{\mathrm{eq}}) + \mu(s_z - s_z^{\mathrm{eq}}) + \nu s_x. \tag{2}$$

Assuming μ was small in their case, they solved (2) at steady state as

$$i_z^{\text{ss}} = i_z^{\text{eq}} - (\nu/\lambda)s_x^{\text{ss}}, \tag{3}$$

which explained the similarity between the field profile of the enhancement and the dispersive EPR line.

The next installment of *Comptes rendus* from April 14, 1958, contained Abragam and Proctor's report "A new method for dynamic polarization of atomic nuclei in solids" (Abragam and Proctor, 1958), which was printed 132 pages after Erb et al. (1958a). This seminal contribution provided the theoretical understanding, and subsequently also the name, of the solid-state effect of dynamic nuclear polarization (DNP). In particular, the authors argued that the excitation of the forbidden transitions $(++) \rightleftharpoons (--)$ and $(+-) \rightleftharpoons (-+)$, which become weakly allowed because the dipolar coupling yields mixed states of the form $(--) + q(-+)$, could be used for DNP. ($\pm$ are the states of the two spin types, both taken as 1/2 for simplicity.) As an experimental verification of the theoretical proposal, the Boltzmann polarization of ^{19}F nuclei was used to enhance the NMR signal of ^{6}Li in a LiF monocrystal, thus demonstrating polarization transfer from nuclei with larger to nuclei with smaller gyromagnetic ratios (i.e., a *nuclear* solid effect).

The parameter of mixing of the Zeeman energy levels, obtained from first-order perturbation theory under the assumption that the dipole-dipole interaction with the electron is much smaller than the nuclear splitting (Abragam, 1955) is

$$q = \frac{1}{4} \frac{D_{\text{dip}}}{\omega_I} \frac{-3\cos\theta\sin\theta\, e^{i\phi}}{r^3}. \tag{4}$$

Here ω_I is the nuclear Larmor frequency, $D_{\text{dip}} = (\mu_0/4\pi)\hbar\gamma_S\gamma_I$ is the dipolar constant, and (r, θ, ϕ) are the spherical polar coordinates of the relative position vector of the spins. The probability amplitude to excite a zero-quantum (ZQ) or double-quantum (DQ) transition between the mixed energy levels is then proportional to $\omega_1 q$, where ω_1 is the mw nutation frequency. Combining the probability of excitation with the Lorentzian spread of the electronic energy levels, as reflected by the homogeneous width of the EPR line, one arrives at the rates of the ZQ and DQ transitions (Wind et al., 1985):

$$v_{0,2}(\Omega) = 4(q^*q)\, v_1(\Omega \pm \omega_I) \tag{5}$$

(the upper sign belongs to v_0 and the lower to v_2), where

$$v_1(\Omega) = \frac{1}{2}\omega_1^2 \frac{R_{2S}}{R_{2S}^2 + \Omega^2} \tag{6}$$

is the rate of the allowed (single-quantum) EPR transition. In these expressions, $\Omega = \omega_S - \omega$ is the offset of the mw frequency ω from the electronic resonance frequency ω_S, and R_{2S} is the electronic T_2 relaxation rate. In essence, the rates of the forbidden transitions are obtained by shifting the rate of the allowed transition by $\pm\omega_I$ along the frequency axis and multiplying by $4|q|^2$.

One month and a half after Abragam and Proctor's report, in the May 28, 1958 issue of *Comptes rendus*, Erb, Motchane and Uebersfeld published another report with the lengthy title "On a new method of nuclear polarization in fluids adsorbed on charcoal. Extension to solids and in particular to irradiated organic substances" (Erb et al., 1958b). There, the authors state (our translation)

The experiments [Erb et al. (1958a)] had been carried out with charcoal whose half-linewidth was 5 gauss and the multiplication factor seemed to reproduce the paramagnetic dispersion curve.

The new experiments [. . .] indicated that the increase in polarization of the proton in the adsorbed fluid is max-imum in all cases, when the electronic and nuclear frequencies are chosen such that the nuclear resonance field differs from the electron resonance field $\delta H = \pm 5$ gauss (within 10%).

These results support the suggestion of Abragam that the new theory of Abragam and Proctor on the nuclear polarization in solids (Abragam and Proctor, 1958) must apply to these new phenomena, and invalidates the inter-pretation proposed previously (Erb et al., 1958a).

The value of 5 gauss found in the case of the proton indeed corresponds to the value deduced from the theoretical formula $H_0 \pm \delta H = (\omega \pm \omega_{\mathrm{N}})/\gamma_e, \ldots$.

This seems to have sealed the fate of the insightful observation of Erb, Motchane, and Uebersfeld (Erb et al., 1958a) that the odd parity of the solid-effect DNP field profile resembles the dispersive component of the EPR line. In the mean time, Abragam's explanation of the solid-state effect in terms of level mixing has become deeply embedded in the thinking of the modern-day DNP researcher, whose quantitative analysis of the experimental data starts with the mixing parameter q (Wind et al., 1985).

In this paper we demonstrate that eq. (2) is correct. We show that the DNP field profile is odd in the field offset for the same reason that the dispersive component of the EPR line is odd, as intuited by Erb, Motchane and Uebersfeld (Erb et al., 1958a). In fact, one could justifiably say that s_x and s_y are indeed responsible for the solid effect, exactly as described in (1). The contribution of s_y does become negligible at lower mw powers or higher magnetic fields, where the solid effect is solely due to the dispersive component, in agreement with (2).

To arrive at these results we depart from the static picture of the solid effect, in which the ratio of the dipolar and nuclear Zeeman interaction energies serves as a perturbation parameter (eq. (4)). In this approach the rates of the forbidden transitions acquire a factor of ω_I^{-2} from $|q|^2$, and a factor of ω_1^2 from the mw excitation (eq. (6)), without any room for non-trivial cross-talk between these two frequencies. Such cross-talk is also not provided by the Lorentzian dependence on Ω.

Instead, starting with the Liouville-von Neumann equation of the density matrix, we obtain equations of motion for the expectation values of the spin operators that are relevant to the solid effect. We identify the rates of the forbidden transitions by analyzing the steady state of these dynamical equations. The resulting analytical expressions are exact, and like the classical expressions (eq. (5)) contain the squares of the dipolar interaction and of ω_1 as multiplicative factors. Their offset dependence, however, couples ω_1 and ω_I in a non-trivial way, which reduces to the classical expressions when $\omega_1 \ll \omega_I$ but predicts qualitatively different dependence when ω_1 is similar to or larger than ω_I. Given the large mw powers currently used in DNP, $\omega_1 \approx \omega_I$ should hold at X band (Neudert et al., 2016) and to a lesser degree at Q band.

The main visual understanding that arises from our dynamical analysis can be summarized as follows. In the solid effect, the transfer of polarization from the electron to the nucleus is mediated by several coherences of two different types: (i) purely electronic and (ii) containing both the electronic and nuclear spin operators. The former act as a Lorentzian band-pass
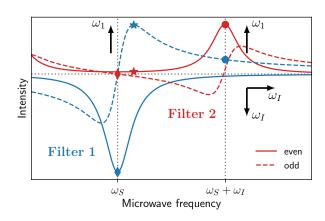
Figure 1. Two band-pass filters centered at ω_S (blue) and $\omega_S \pm \omega_I$ (red). The solid effect efficiency is proportional to the product of the even (with respect to ω_S) component of one of the filters and the odd component of the other filter, since the two filters are connected in series. Increasing the mw power (ω_1) increases the intensities of both filters, thus their product grows quadratically. Increasing the magnetic field (ω_I) decreases the intensity of the second filter and shifts it to the right, thus quadratically decreasing the overlap with the first filter. The second filter has another symmetrical component centered at $\omega_S - \omega_I$ which is not shown.

90 filter centered at the electronic Larmor frequency; the latter as two (approximately) Lorentzian band-pass filters centered at $\omega \approx \omega_S \pm \omega_I$. These filters are depicted in fig. 1, which shows only half of the second filter for clarity. The polarization transfer efficiency depends on the overlap (i.e., product) of the two filters since they are connected in series.

The classical expression for the forbidden transition rates (eqs. (5) and (6)) accounts only for the even part of the second filter (solid red line in fig. 1). According to our picture, this even component has to be multiplied by the imaginary (odd) part
95 of the first filter (dashed blue line) which is nothing but the dispersive EPR line that Erb, Motchane and Uebersfeld suspected to play a central role in the solid effect. At the canonical offset of the solid effect, $\omega_S + \omega_I$, this corresponds to the product of the blue and red filled circles in fig. 1.

Since multiplication is commutative, in this mental picture there is an apparent duality between the two types of filters. The colored circles in fig. 1 are at the maximum of the even part of the red filter, which is multiplied by the odd part of the blue filter.
100 But for the solid effect one also multiplies the odd part of the red filter with the even part of the blue filter. At the maximum of the latter (blue diamond) the odd part of the red filter equals zero (red diamond). As a result, the solid effect is observed at $\omega_S \pm \omega_I$ but not at ω_S.

The amplitudes of the solid red line and dashed blue line increase linearly with ω_1, hence their overlap at $\omega_S + \omega_I$ scales with ω_1^2. The amplitude of the solid red line decreases linearly with ω_I. Since ω_I also changes the distance of this filter from
105 the electronic filter, the overlap at $\omega_S + \omega_I$ scales inversely with ω_I^2. This is how the factor ω_1^2/ω_I^2, which in the classical description resulted from substituting (4) and (6) into (5), arises in our picture.

The theoretical justification and details of this alternative description of the solid effect are presented in the following sections. We start with an overview of the rate equations of the electronic and nuclear polarizations, and connect their steady

state to the DNP enhancement (Sec. 2). The focus here is on the phenomenological rate constants used to describe the forbidden
transitions. After that, in Sec. 3, we derive quantum-mechanical equations of motion for the spin operators of relevance to the
solid effect. In Sec. 4 we require that these equations of motion and the rate equations of Sec. 2 have identical steady states.
This allows us to express the phenomenological rate constants in terms of the parameters of the problem. In Sec. 5 we examine
the relationship between the classical expression of the forbidden transition rates (eq. (5)) and our results. Our conclusions are
given in Sec. 6.

Differently from the static picture based on level mixing and perturbation theory, the dynamical description developed here
is readily extendable to liquids (Erb et al., 1958a; Leblond et al., 1971; Gizatullin et al., 2022; Kuzhelev et al., 2022) where
the dipolar interaction is time-dependent. Such extension is presented in the companion paper (Paper II). There we show that
the random molecular motions in liquids broaden the second filter in fig. 1, thus decreasing its amplitude at $\omega_S + \omega_I$. This
substantially reduces the product at the position of the red and blue filled circles, and hence the efficiency of the solid effect.
At the same time, however, the motional broadening increases the tail of the solid red line at the location where the dispersive
EPR component (dashed blue line) has a maximum. As a result, the product of the two amplitudes at the positions of the
blue and red stars in fig. 1 may become sufficiently large to be manifested in the DNP field profile. One then sees solid-effect
enhancements at "wrong" offsets, in addition to the enhancements at the "correct" solid-effect offsets (Kuzhelev et al., 2022).
Under such conditions, the dispersive component of the EPR line is manifested in the solid-effect DNP field profile, visually
confirming the hunch of Erb, Motchane and Uebersfeld (Erb et al., 1958a).

2 Rate equations

In the rate-equation treatment of DNP (Abragam, 1955; Webb, 1961; Barker, 1962) both thermal relaxation and mw excitation
are envisioned as flipping spins between pairs of energy levels with certain rates, as depicted in figs. 2a and 2b. Excitation of the
allowed EPR transition (fig. 2a) does not lead to simultaneous flips of the electronic and nuclear spins, and is thus not capable
of transferring polarization from the former to the latter. In contrast, the ZQ and DQ forbidden transitions involve simultaneous
electron-nucleus spin flips (fig. 2b), and drive the solid-state DNP effect which is analyzed in this paper.

2.1 Derivation of the rate equations

While the forbidden transitions couple the nuclear and electronic polarizations, their influence on the latter is typically negli-
gible compared to other mechanisms of electronic relaxation. It is therefore justified to write a rate equation for the electronic
polarization considering only the allowed EPR transition.

Below, we first examine the electronic transition on its own (fig. 2a) and then turn to the electron-nucleus transitions (fig.
2b). The derivation of the rate equations is illustrated only for the mw excitation. Relaxation is included at the end by analogy.

MAGNETIC RESONANCE
Open Access Discussions

2.1.1 Allowed electronic transition

Let n_+ and n_- be the populations of the two electronic spin energy levels in fig. 2a. Assuming the spins are not destroyed or created, the sum of the two populations is constant in time. Treating the mw excitation as a process that randomly flips the spins with rate constant v_1, we have

$$\dot{n}_+|_{\mathrm{mw}} = -\dot{n}_-|_{\mathrm{mw}} = -v_1(n_+ - n_-). \tag{7}$$

(The subscript of the vertical bar indicates that the time derivative accounts only for mw excitation.) Note that $v_1 \geq 0$, since a negative rate constant does not make physical sense.

The electron spin polarization $P_S = (n_+ - n_-)/(n_+ + n_-)$ is negative at thermal equilibrium, i.e., $P_S^{\mathrm{eq}} < 0$. Differentiating P_S with respect to time and using (7), we find $\dot{P}_S|_{\mathrm{mw}} = -2v_1 P_S$.

The action of thermal relaxation is analogous but P_S decays towards its thermal equilibrium with rate $2w_{1S} = R_{1S} = 1/T_{1S}$, where T_{1S} is the electronic T_1 relaxation time. Combining mw excitation and thermal relaxation we obtain the following rate equation for the electronic polarization:

$$\dot{P}_S = -R_{1S}(P_S - P_S^{\mathrm{eq}}) - 2v_1 P_S. \tag{8}$$

Equation (8) is depicted in fig. 2c. In this graphical representation of the differential equation, we use an oval node to represent a dynamical variable (P_S in this case) whose time derivative is calculated by summing the contributions of all arrows that point *into* the node. The contribution of an arrow is obtained by multiplying the weight of the arrow by the variable from which the arrow *originates*. Differently from similar graphical representations in chemical kinetics, here an arrow does not deplete the node at its origin but only contributes to the node at its pointed end. By shading a node in gray we indicate that the corresponding variable remains constant in time. Each arrow in fig. 2c corresponds to one of the summands on the right-hand side of (8). The two gray arrows account for thermal relaxation and the red arrow for mw excitation.

We refer to arrows that leave a node and enter the same node as self-arrows. To prevent positive feedback, and thus ensure dynamical stability, the total contribution of all self-arrows of a node should not be positive. For the electronic polarization this means $R_{1S} + 2v_1 \geq 0$. (We always write the weight of a self-arrow with an explicit negative sign, which is placed inside the loop formed by the arrow.)

2.1.2 Forbidden transitions

Now we turn to the four-level system in fig. 2b. Let n_{++}, n_{+-}, n_{-+} and n_{--} be the populations of the levels. While their sum, $n = n_{++} + n_{+-} + n_{-+} + n_{--}$, remains constant in time, the individual populations change due to ZQ and DQ transitions with rate constants v_0 and v_2 as follows:

$$\dot{n}_{-+}|_{\mathrm{mw}} = -\dot{n}_{+-}|_{\mathrm{mw}} = -v_0(n_{-+} - n_{+-})$$

$$\dot{n}_{++}|_{\mathrm{mw}} = -\dot{n}_{--}|_{\mathrm{mw}} = -v_2(n_{++} - n_{--}). \tag{9}$$

It is implicitly assumed that $v_0 \geq 0$ and $v_2 \geq 0$, as negative rate constants would not make physical sense.
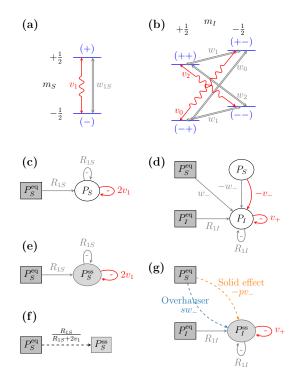
Figure 2. Energy levels of (**a**) single electronic spin ($S = 1/2$) and (**b**) one electronic spin and one nuclear spin ($I = 1/2$). Diagrammatic representation of the rate equations of (**c**) the electronic and (**d**) nuclear polarizations. (**e**) Rate equation of the electronic polarization at steady state and (**f**) its solution. (**g**) Rate equation of the nuclear polarization at steady state. (a,b) Microwaves excite single-, zero- and double-quantum transitions (wiggly red arrows) with rate constants v_1, v_0, and v_2. Thermal relaxation (thick grey arrows) arises from coupling to external degrees of freedom, e.g., motion. (c-g) An arrow flowing into a node contributes either to the time derivative of the variable (oval node) or directly to the variable (rectangular node). A gray node indicates that the variable is constant in time. (e,g) The sum of the arrows flowing into a gray oval node equals zero. (f,g) Dashed arrows are deduced relationships between the variables at steady state.

The polarizations of the nuclear and electronic spins are

$$P_I = [(n_{++} - n_{+-}) + (n_{-+} - n_{--})]/n$$
$$P_S = [(n_{++} - n_{-+}) + (n_{+-} - n_{--})]/n. \tag{10}$$

170 While, as before, $P_S^{\text{eq}} < 0$, the sign of P_I at thermal equilibrium will depend on the gyromagnetic ratio of the nuclear spin. We will assume protons, hence $\gamma_I > 0$ and $P_I^{\text{eq}} > 0$.

Differentiating P_I with respect to time and using (9), we obtain

$$\dot{P}_I|_{\text{mw}} = -(v_2 + v_0)P_I - (v_2 - v_0)P_S, \tag{11}$$

which shows that mw excitation of the forbidden transitions couples the evolution of the nuclear polarization to the polarization
175 of the electrons. This coupling is responsible for the solid-state DNP effect.

MAGNETIC RESONANCE
Discussions
Open Access

Because one always encounters either the difference or the sum of the ZQ and DQ rate constants, we introduce

$$v_\pm = v_2 \pm v_0. \tag{12}$$

In fact, as we show later, the individual rates v_0 and v_2 may become negative, and thus meaningless from the rate-equation point of view.

180 The two terms on the right-hand side of (11) are represented by the two red arrows in fig. 2d. (The gray arrows correspond to thermal relaxation which is considered below.) For dynamical stability, $R_{1I} + v_+ \geq 0$.

Of main interest for the current paper are the rates that describe the effect of the microwaves (i.e., the red arrows in fig. 2). Nevertheless, we also discuss thermal relaxation as it is essential for reaching steady state.

Thermal relaxation of the nuclear spins due to their coupling to the electronic spins acts analogously to (11) after replacing

185 the rates $v_{0,2}$ by $w_{0,2}$ and the polarizations by their deviations from thermal equilibrium. Further including nuclear T_1 relaxation due to mechanisms other than the coupling to the electrons, we arrive at

$$\dot{P}_I|_{\text{th}} = -R_{1I}^0(P_I - P_I^{\text{eq}}) - 2w_1(P_I - P_I^{\text{eq}})$$
$$\quad - w_+(P_I - P_I^{\text{eq}}) - w_-(P_S - P_S^{\text{eq}}), \tag{13}$$

where R_{1I}^0 is the nuclear T_1 relaxation rate in the absence of the polarizing agent, and

$$w_\pm = w_2 \pm w_0 \tag{14}$$

190 analogously to (12). The cross-relaxation rate w_- is seen to couple the dynamics of P_I to P_S. This coupling is responsible for the Overhauser DNP effect.

From (13), the total nuclear T_1 relaxation rate (i.e., in the presence of the free radical) is identified as $R_{1I} = R_{1I}^0 + 2w_1 + w_+$. Combining the contributions of mw excitation (eq. (11)) and relaxation (eq. (13)), we arrive at the following rate equation for the nuclear polarization:

$$\dot{P}_I = -R_{1I}(P_I - P_I^{\text{eq}}) - w_-(P_S - P_S^{\text{eq}})$$
195 $$\quad - v_+P_I - v_-P_S. \tag{15}$$

This is the full differential equation depicted in fig. 2d.

2.2 Steady state of the rate equations

Although the rate equations (8) and (15) describe the evolution of the electronic and nuclear polarizations in time, one is almost exclusively interested in their steady state (Webb, 1961). In fact, the only use of the rate equations appears to be in their steady

200 state.

At steady state the time derivatives vanish and the dynamical variables settle at constant values, which we denote with the superscript 'ss'. In our diagrams, the node of a constant variable is shaded gray. Thus a gray oval node implies that the sum of all inflowing arrows equals zero. With this understanding, fig. 2e represents the rate equation of P_S at steady state.

Since the dynamics of the electronic polarization is decoupled from the polarization of the nuclei, the steady state of (8) can
205 be analyzed on its own. The condition that all inflowing arrows sum to zero yields

$$P_S^{\text{ss}} = \frac{R_{1S}}{R_{1S} + 2v_1} P_S^{\text{eq}} = p P_S^{\text{eq}}, \tag{16}$$

where the second equality defines the factor p. (Observe how the weights of the two self-arrows in fig. 2e end up in the denominator.) This steady-state solution is depicted in fig. 2f.

We use a rectangular node when the inflowing arrows contribute directly to the value of the variable inside the node. (In
210 contrast, when a variable is inside an oval node the arrows contribute to its time derivative.) The distinction between solid arrows and dashed arrows is that the former are reserved for fundamental, causal relationships between the variables which dictate their dynamics at all times, while the dashed arrows indicate deduced mathematical relationships at steady state, which need not reflect direct causal links.

We will view the dashed arrow in fig. 2f as a transfer function that multiplies the variable at its input to produce the variable
215 at its output. In this case the transfer function is $p = 1 - s$, where s is the familiar saturation factor of the (allowed) electronic transition. Since p quantifies how close the steady-state polarization is to its Boltzmann value (eq. (16)), we call it the electronic polarization factor, and use it interchangeably with $1 - s$.

Before turning to the steady state of the nuclear polarization, we observe that P_S and P_I reach steady state on time scales of the order of T_{1S} and T_{1I}, respectively. Since T_{1S} is typically much shorter than T_{1I}, there must be intermediate times where
220 P_S has already reached steady state but P_I has not. Thus, it should be possible to replace P_S by P_S^{ss} in the rate equation of the nuclear polarization (eq. (15)). Further using (16), we have

$$\dot{P}_I = -R_{1I}(P_I - P_I^{\text{eq}}) + s w_- P_S^{\text{eq}} - v_+ P_I - p v_- P_S^{\text{eq}}. \tag{17}$$

This rate equation at steady state is depicted in fig. 2g.

There are two links from P_S^{eq} to the derivative of P_I^{ss}. One of them scales with s and relies on the efficient saturation of the
225 allowed EPR transition; the other scales with $p = 1 - s$. These two pathways correspond to the Overhauser and the solid-state DNP effects, respectively.

Solving the steady state of (17) for the nuclear polarization, we get

$$P_I^{\text{ss}} = p_X \left[P_I^{\text{eq}} + \frac{s w_-}{R_{1I}} P_S^{\text{eq}} - \frac{p v_-}{R_{1I}} P_S^{\text{eq}} \right], \tag{18}$$

where we have defined the factor

230 $$p_X = \frac{R_{1I}}{R_{1I} + v_+}. \tag{19}$$

Because of its similarity to p in (16), we refer to p_X as the nuclear cross-polarization factor. Clearly, for large steady-state nuclear polarization, p_X should be as large as possible.

DNP is generally quantified through the enhancement of the nuclear polarization,

$$\epsilon = P_I^{\text{ss}} / P_I^{\text{eq}} - 1, \tag{20}$$

MAGNETIC RESONANCE
Open Access Discussions

235 which is defined such that it equals zero at thermal equilibrium. Taking into account that $P_S^{\text{eq}}/P_I^{\text{eq}} = -|\gamma_S|/\gamma_I$, from (18) we obtain

$$\epsilon = \epsilon_X + \epsilon_{\text{OE}} + \epsilon_{\text{SE}}, \tag{21}$$

where we have introduced the following additive contributions to the DNP enhancement:

$$\epsilon_{\text{SE}} = p_X \frac{pv_-}{R_{1I}} \frac{|\gamma_S|}{\gamma_I}, \qquad \epsilon_{\text{OE}} = -p_X \frac{sw_-}{R_{1I}} \frac{|\gamma_S|}{\gamma_I}$$

$$\epsilon_X = p_X - 1. \tag{22}$$

240 The first two correspond to the solid and Overhauser effects. The last one is due to neither of them. When $p_X \neq 1$ (i.e., $v_+ \neq 0$) this term can shift the final enhancement by about one unit at most, and should be negligible in most cases of practical interest.

3 Spin dynamics

The above rate-equation analysis identified how different factors contribute to the DNP enhancement. However, for a quantitative understanding of the solid effect it is necessary to know how the excitation rate constants v_1 and $v_\pm$ depend on the various

245 experimental parameters. Such expressions are obtained in Sec. 4 after we analyze the relevant spin dynamics in the present section.

Quantum mechanically the polarizations P_S and P_I correspond to the expectations of the electronic and nuclear spin operators S_z and I_z. The coherent evolution of the expectation value $q = \langle Q \rangle$ of a general spin operator Q, under the action of a spin Hamiltonian H (in units of angular frequency) is given by (Abragam, 1961)

250 $$\dot{q}|_{\text{coh}} = i\langle [H, Q] \rangle. \tag{23}$$

In this section we use (23) to obtain equations of motion for the expectation values of the operators relevant to the solid effect. As in the previous section, we first analyze the electronic spins, and tackle the coupled electronic and nuclear spins after that.

3.1 Bloch equations

The interaction of the electronic spins with the magnetic field is described by the Hamiltonian

255 $$H = \Omega S_z + \omega_1 S_x, \tag{24}$$

where the first term accounts for the Zeeman interaction with the constant magnetic field B_0, and the second term for the interaction with the mw field B_1. The offset frequency $\Omega = \omega_S - \omega$ appears because the Hamiltonian is in the rotating frame.

Using (23) with the Hamiltonian (24), one can determine the coherent dynamics of $s_z = \langle S_z \rangle$, $s_y = \langle S_y \rangle$ and $s_x = \langle S_x \rangle$. After appending electronic T_1 and T_2 relaxation by hand, one obtains the familiar Bloch equations

$$\dot{s}_x = -\Omega s_y - R_{2S} s_x$$

$$\dot{s}_y = \Omega s_x - \omega_1 s_z - R_{2S} s_y$$

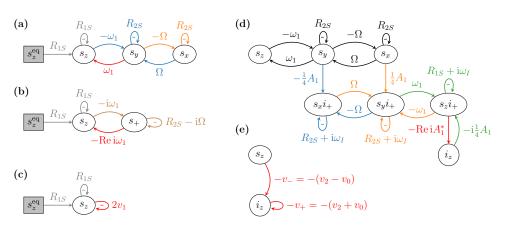260 $$\dot{s}_z = \omega_1 s_y - R_{1S} s_z + R_{1S} s_z^{\text{eq}}. \tag{25}$$

Figure 3. (**a**) Real-valued and (**b**) complex-valued classical Bloch equations and (**c**) corresponding dynamics according to the rate equation of the electronic polarization. (**d**) Spin dynamics of relevance to the solid effect and (**e**) corresponding dynamics implied by the rate equation of the nuclear polarization.

These are depicted in fig. 3a.

The two orange arrows in the figure correspond to the right-hand side of the first equation in (25) and the three blue arrows to the second equation. The self-arrows of the oval nodes are due to T_1 and T_2 relaxation. The offset frequency leads to rotation in the x-y plane with angular velocity Ω. This corresponds to the loop formed by the orange and blue arrows with weights $-\Omega$ and $+\Omega$. Similarly, the loop formed by the blue and red arrows with weights $-\omega_1$ and $+\omega_1$ indicates rotation in the y-z plane with angular velocity ω_1 due to the mw excitation.

Alternatively, one can form the dynamical variable $s_+ = s_x + \mathrm{i}s_y$ and work with the complex-valued Bloch equations

$$\dot{s}_+ = -(R_{2S} - \mathrm{i}\Omega)s_+ - \mathrm{i}\omega_1 s_z$$
$$\dot{s}_z = -R_{1S}(s_z - s_z^{\mathrm{eq}}) - \mathrm{Re}\{\mathrm{i}\omega_1 s_+\} \tag{26}$$

which are depicted in fig. 3b. Notably, the rotation in the x-y plane with angular velocity Ω has now become the imaginary part of the self-arrow of s_+ whose real part is the T_2 relaxation rate.

In the complex-valued Bloch equations we have arbitrarily retained s_+ and dropped s_-. Reducing the number of variables in this way simplifies the diagrammatic representation in fig. 3b compared to fig. 3a. (The simplification will be more substantial when we move to the analysis of the coupled electron-nucleus system.) Note however that the contribution of s_- is recovered when the real part of $\mathrm{i}s_+$ is used to calculate the time derivative of s_z in the second line of (26).

In fig. 3c we recall the dynamics of s_z implied by the rate equation of the electronic polarization (fig. 2c). The visual comparison of this dynamics with the Bloch equations above it makes clear that the rate v_1 of the allowed EPR transition is supposed to account in some effective way for the coupling between s_z and s_y (due to ω_1), and for the dynamics of the transverse components (due to Ω and R_{2S}). The rate constant v_1 is thus expected to be a function of ω_1, Ω and R_{2S}.

MAGNETIC RESONANCE
Open Access

Discussions

3.2 Generalization to two coupled Bloch equations

280 To carry out a similar analysis for the nuclear polarization, we consider the spin Hamiltonian (Wenckebach, 2016)

$$H = \Omega S_z + \omega_1 S_x - \omega_I I_z + \frac{1}{2}(A_1^* S_z I_+ + A_1 S_z I_-), \tag{27}$$

which is in the rotating frame for the electronic spin and in the laboratory frame for the nuclear spin. The first two terms are the same as in the Hamiltonian (24). The third term describes the nuclear Zeeman interaction. The sign of ω_I is negative since we assumed a nuclear spin with positive gyromagnetic ratio.

285   The last two terms in the Hamiltonian account for the dipolar interaction between the electronic and nuclear spins. We have truncated this interaction by dropping all non-secular terms containing S_x and S_y. Similar to the assumption behind the derivation of the mixing factor (eq. (4)), we take the dipolar interaction to be small compared to the nuclear Zeeman splitting and drop the secular term proportional to $S_z I_z$. The remaining, pseudosecular terms scale with the dipolar coupling (Wenckebach, 2016)

290 $$A_1 = D_{\mathrm{dip}}\frac{-3\cos\theta\sin\theta}{r^3}\mathrm{e}^{\mathrm{i}\phi} \tag{28}$$

where $D_{\mathrm{dip}}/2\pi \approx 79.066\,\mathrm{kHz\,nm^3}$ for protons. The subscript of A_1 indicates that its angular dependence is identical to the second-degree spherical harmonic of order $m = 1$.

We start our derivation of equations of motion with $i_z = \langle I_z \rangle$, as it corresponds to the nuclear polarization. There is no contribution from the first three terms in the Hamiltonian (27) as I_z commutes with all of them (eq. (23)). From the commutator
295 with the dipolar terms we obtain

$$\dot{i}_z|_{\mathrm{coh}} = \mathrm{i}\frac{1}{2}(A_1 g_z^* - A_1^* g_z) = -\mathrm{Re}\{\mathrm{i}A_1^* g_z\}, \tag{29}$$

where

$$g_n = \langle S_n I_+ \rangle \qquad (n = x, y, z). \tag{30}$$

Proceeding in the same way, we first find

300 $$\dot{g}_z|_{\mathrm{coh}} = -\mathrm{i}\omega_I g_z + \omega_1 g_y - \mathrm{i}(A_1/4)i_z \tag{31}$$

and then

$$\dot{g}_y|_{\mathrm{coh}} = \Omega g_x - \mathrm{i}\omega_I g_y - \omega_1 g_z + (A_1/4)s_x$$
$$\dot{g}_x|_{\mathrm{coh}} = -\mathrm{i}\omega_I g_x - \Omega g_y - (A_1/4)s_y. \tag{32}$$

The chain of dynamical equations can be terminated at this stage, as $s_{x,y}$ obey the classical Bloch equations discussed above. (The dynamics of the electronic spin was taken to be independent of its dipolar coupling with the nuclei.)

**MAGNETIC
RESONANCE**
Discussions

305   In addition to the coherent evolution considered so far, $g_z = \langle S_z I_+ \rangle$ and $g_{x,y} = \langle S_{x,y} I_+ \rangle$ are expected to decay with rates $R_{1S} + R_{2I}$ and $R_{2S} + R_{2I}$, respectively. Neglecting R_{2I} compared to R_{1S} and R_{2S}, we arrive at the following system of coupled differential equations:

$$
\begin{bmatrix} \dot{g}_x \\ \dot{g}_y \\ \dot{g}_z \end{bmatrix} = -\mathscr{B} \begin{bmatrix} g_x \\ g_y \\ g_z \end{bmatrix} - \mathrm{i}\frac{1}{4} A_1 \begin{bmatrix} -\mathrm{i}s_y \\ \mathrm{i}s_x \\ i_z \end{bmatrix},
\tag{33}
$$

with

310   $$
\mathscr{B} = \begin{bmatrix} R_{2S} + \mathrm{i}\omega_I & \Omega & 0 \\ -\Omega & R_{2S} + \mathrm{i}\omega_I & \omega_1 \\ 0 & -\omega_1 & R_{1S} + \mathrm{i}\omega_I \end{bmatrix}.
\tag{34}
$$

This matrix is essentially the familiar Bloch matrix of the real-valued Bloch equations (25) but with $\mathrm{i}\omega_I$ added to its main diagonal.

If desired, one can also supplement (29) with nuclear T_1 relaxation. However, because our aim is to identify the forbidden-transition rates $v_\pm$, this is not necessary. In any case, we already analyzed the balance between thermal relaxation and mw

315   excitation at steady state using the rate-equation formalism (Sec. 2.2).

Equations (29) and (33), supplemented by the Bloch equations (25), constitute the generalization of the Bloch equations to the four-level system in fig. 2b as relevant to the solid effect. This system of equations is depicted in fig. 3d, where blue, orange and green arrows flow into the nodes g_x, g_y and g_z, respectively. Black arrows correspond to the classical Bloch equations.

For comparison, in fig. 3e we recall the description of the same spin dynamics according to the rate-equation formalism (red

320   arrows in fig. 2d). Evidently, the two rates $v_\pm$ are expected to summarize in some faithful way the complexity of the proper, quantum-mechanical dynamics in fig. 3d.

The graphical representation of the spin dynamics in fig. 3d provides visual access to many aspects of the solid effect. Regarding the overall organization, we notice that the classical Bloch-equations pattern connecting the top three nodes (black arrows) is recapitulated between the nodes g_n ($n = x, y, z$) below them. As a result, there are two sets of Bloch equations

325   which are connected back to back, with the y variable of one of them feeding into the x variable of the other, and vice versa. The connection between these two set is established by the dipolar coupling (A_1). Due to the involvement of the nuclear spin operator I_+, the second set of Bloch equations is "shifted" by the nuclear Larmor frequency, as evidenced by the imaginary part of the self-arrows of g_n. Although the coherences $S_n I_-$ are not explicitly modeled, their contribution is recovered when we feed the real value of $\mathrm{i}A_1^* g_z$ into the time derivative of i_z. At this stage, $+\omega_I$ and $-\omega_I$ contribute symmetrically.

330   Turning attention to the pathways bridging s_z to i_z, we gain visual understanding of the mechanism of the dynamical coupling between the electronic and nuclear polarizations in the solid effect. Following the "flow" of the arrows, i_z is reached from s_z in four steps (not counting the mixing of the transverse components by $\pm\Omega$). First, the mw excitation (ω_1) generates the transverse components $s_{x,y}$ from s_z. This step is described by the classical Bloch equations. Then, from $s_{x,y}$ the dipolar coupling (A_1) generates the coherences $s_{x,y} i_+$. These are then converted to $s_z i_+$ by the mw excitation, and finally the dipolar

335   interaction transforms $s_z i_+$ to i_z. Because the weights ω_1 and A_1 appear twice along the path from s_z to i_z, the net efficiency of the solid effect scales with the squares of both ω_1 and A_1.

    Additionally, we observe that all paths from s_z to i_z traverse the arrows with weights $\pm\Omega$. Thus, on resonance ($\Omega = 0$) the possibility of polarization transfer is severed. This observation does not appear to be particularly useful as driving the forbidden transitions requires $\Omega \approx \pm\omega_I$ anyway. However, as going along an arrow with weight $\pm\Omega$ amounts to multiplication

340   by Ω, we realize that crossing from the left side of the dynamical network to the right side involves change of parity in Ω. In other words, because s_z is an even function of the frequency offset, its effect on i_z must be odd in Ω. This is the reason for the anti-symmetric field profile of the solid effect (in contrast to the symmetric profile of the Overhauser effect). The diagram makes clear that the solid effect is odd in Ω for the same reason that s_x is odd, as intuited by Erb, Motchane and Uebersfeld (Erb et al., 1958a).

345   The above observations were related to the paths from s_z to i_z, which contribute to the rate v_- (fig. 3e). Examining the paths that contribute to the self-loop with weight v_+, we see that there are two possibilities: one consisting of two steps and the other of four (fig. 3d). The shorter path from i_z to g_z, and back to i_z, relies only on the dipolar coupling between the electronic and nuclear spins and must be active even in the absence of mw excitation. The longer path additionally goes from g_z to $g_{x,y}$ (the latter are mixed by Ω) and back, and contributes only under mw irradiation. Considering the separate treatment of thermal

350   relaxation and mw excitation, we realize that the short loop in fact contributes to the nuclear T_1 relaxation (more precisely to the rate w_1 in fig. 2b), hence its contribution should be removed when calculating the rate v_+.

    These general observations are developed in more detail below.

4   Excitation rate constants

It is clear that the polarization dynamics in fig. 3c could approximate the Bloch equations in fig. 3a only under some special

355   conditions. For example, if the T_{2S} and T_{1S} relaxation times are well separated, it is possible to eliminate the fast variables $s_{x,y}$ from the Bloch equations and thus obtain a closed dynamical equation for the slow variable s_z, which will be valid at times longer than the fast time scale T_{2S} (Van Kampen, 1985). Similarly, the reduced dynamics in fig. 3e could be a good approximation of the true dynamics in fig. 3d under some conditions.

    If, however, the reduced equations are not required to provide a faithful description of the dynamics, there is a regime in

360   which they are exact without any additional requirements. This is the regime of steady state. In fact, since the use of the rate equations from Sec. 2 lies in the steady state that they describe, and not in the dynamics that they unwittingly imply, nothing is sacrificed by confining them to steady state.

    In this section we analyze the steady state of the quantum-mechanical equations of motion (Sec. 3) and compare it with the steady state of the rate equations (Sec. 2.2). The comparison will allow us to identify the phenomenological rate constants v_1,

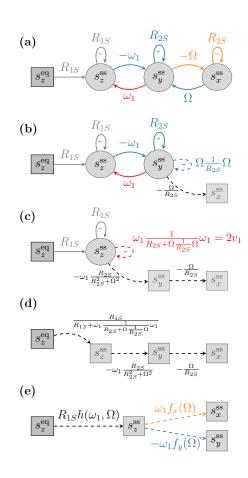365 $v_\pm$ in terms of the parameters of the spin dynamics.

Figure 4. (**a**) Real-valued Bloch equations at steady state. (**b**) Elimination of s_x^{ss}. (**c**) Further elimination of s_y^{ss}. (**d**) Solution for s_z^{ss}. (**e**) Steady-state solution of the Bloch equations with the dashed arrows viewed as transfer functions.

4.1 Steady state of the Bloch equations

At steady state, the sum of all arrows flowing into an oval node equals zero. Shading the oval nodes in fig. 3a in gray, we arrive at fig. 4a which represents the classical Bloch equations at steady state. The condition that the two orange arrows flowing into s_x^{ss} sum to zero yields

$$s_x^{\mathrm{ss}} = -\frac{\Omega}{R_{2S}} s_y^{\mathrm{ss}}. \tag{35}$$

(Observe how the weight of the self arrow of s_x^{ss} ends up in the denominator.) This steady-state relationship is depicted by the black dashed arrow in fig. 4b.

Using (35) one can eliminate s_x^{ss} from the differential equation of s_y (second equation in (25)). The remaining two equations, which contain only the variables s_y^{ss} and s_z^{ss}, are represented in fig. 4b. The elimination of s_x^{ss} resulted in the self-arrow of s_y^{ss} drawn with a dashed blue line.

Proceeding further, we now express s_y^{ss} in terms of s_z^{ss} using the second Bloch equation in (25):

$$s_y^{\mathrm{ss}} = -\frac{\omega_1}{R_{2S} + \Omega \frac{1}{R_{2S}} \Omega} s_z^{\mathrm{ss}}. \tag{36}$$

(Again the self-arrows of the eliminated node end up in the denominator.) This relation is represented by the black dashed arrow in fig. 4c. Using (36) we now eliminate s_y^{ss} from the equation of s_z^{ss} (last equation in (25)). The term that contained s_y^{ss}

380   corresponds to the self-arrow of s_z^{ss} which is shown with red dashed arrow in fig. 4c.

Visual comparison of the remaining equation of s_z^{ss} (fig. 4c) with fig. 3c directly yields

$$v_1 = \frac{1}{2} \omega_1^2 \frac{R_{2S}}{R_{2S}^2 + \Omega^2} \tag{37}$$

for the rate constant of the allowed EPR transition. This result agrees with (6). Our derivation makes clear that this functional dependence of v_1 on ω_1, R_{2S} and Ω is, in fact, exact at steady state.

385   If the purpose is to determine the rate constant v_1, the analysis can be terminated at this point without ever encountering the T_1 relaxation of the electronic spins. Below, when we determine the rates $v_\pm$, we will similarly need to consider only the coherent evolution of i_z without worrying about the nuclear T_1 relaxation. In fact, once the rate constants of mw excitation are identified, the steady-state analysis is identical to the one we already carried out in Sec. 2 for the rate equations of the polarizations.

390   For completeness, here we proceed one step further and solve the equation for s_z^{ss} by moving the self-arrows in fig. 4c to the denominator:

$$s_z^{\mathrm{ss}} = \frac{R_{1S}}{R_{1S} + \omega_1 \frac{1}{R_{2S} + \Omega \frac{1}{R_{2S}} \Omega} \omega_1} s_z^{\mathrm{eq}}. \tag{38}$$

This result (fig. 4d) is equivalent to (16).

The above successive elimination of the variables from the steady-state Bloch equations (figs. 4b-d) is just the poor man's

395   inversion of the Bloch matrix. Nevertheless, it allowed us to follow the step-by-step emergence of the functions

$$f_y(\Omega) = \frac{1}{R_{2S} + \Omega \frac{1}{R_{2S}} \Omega}, \quad f_x(\Omega) = \frac{\Omega}{R_{2S}} f_y(\Omega)$$

$$h(\omega_1, \Omega) = \frac{1}{R_{1S} + \omega_1 f_y(\Omega) \omega_1}, \tag{39}$$

which have units of time (Table 1, first row). In terms of these functions, the ratios between the variables of the Bloch equations at steady state are

$$\frac{s_{x,y}^{\mathrm{ss}}}{s_z^{\mathrm{ss}}} = \pm \omega_1 f_{x,y}(\Omega), \quad \frac{s_z^{\mathrm{ss}}}{s_z^{\mathrm{eq}}} = R_{1S} h(\omega_1, \Omega) = p. \tag{40}$$

400   (The last equality follows from (16).) These ratios are depicted as transfer functions in fig. 4e. Note that the weights of the dashed arrows are dimensionless, as they equal the product of a variable with units of inverse time and a function with units of time (Table 1, second row). For our purposes it will be convenient to think of the steady-state Bloch equations as a system that takes s_z^{eq} as an input and produces the outputs $s_{x,y}^{\mathrm{ss}}$, as suggested graphically in fig. 4e.

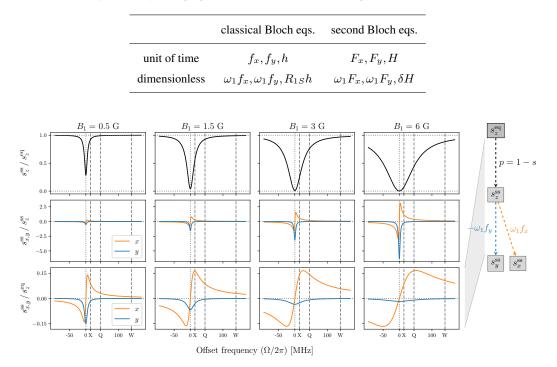**Table 1.** Functions characterizing the steady-state properties of the two sets of Bloch equations.

	classical Bloch eqs.	second Bloch eqs.
unit of time	f_x, f_y, h	F_x, F_y, H
dimensionless	$\omega_1 f_x, \omega_1 f_y, R_{1S} h$	$\omega_1 F_x, \omega_1 F_y, \delta H$

Figure 5. Transfer functions at the steady state of the classical Bloch equations. The conversion of B_1 to ω_1 was for free radical with $g = 2$, hence $B_1 = 6\,\mathrm{G}$ corresponds to $\omega_1/2\pi = 16.8\,\mathrm{MHz}$. In all plots $T_2 = 60\,\mathrm{ns}$ and $T_1 = 9\,T_2$. The positions of the nuclear Larmor frequencies at X (14 MHz), Q (45 MHz) and W (140 MHz) bands are indicated with vertical dashed lines.

To examine the properties of this system, in fig. 5 we plot its transfer functions (40) against the offset frequency for four different values of B_1. A free radical with $g = 2$ was assumed when converting B_1 to ω_1, so that $B_1 = 6\,\mathrm{G}$ corresponds to $\omega_1/2\pi = 16.8\,\mathrm{MHz}$. This maximum value of B_1 is intended to reflect the actual mw field of modern-day DNP spectrometers at X band (Neudert et al., 2016) and at J band (Kuzhelev et al., 2022). The electronic relaxation times used in the plots were $T_{2S} = 60\,\mathrm{ns}$ and $T_{1S} = 9\,T_{2S}$.

The first row of fig. 5 shows the transfer function $R_{1S} h$, which is the electronic polarization factor under mw power. The saturation is most efficient on resonance ($\Omega = 0$) and quickly becomes inefficient at larger offsets. With increasing mw power the deviation of s_z^{ss} from equilibrium spreads to larger offsets.

As our main interest is in the solid effect, we have indicated with dashed vertical lines the offsets Ω that correspond to the nuclear Larmor frequencies of a proton spin at the X (9.2 GHz/14 MHz), Q (30 GHz/45 MHz) and W (92 GHz/140 MHz) mw bands. Considering that DNP is performed at high mw powers, let us examine the saturation at $B_1 = 6\,\mathrm{G}$ (fig. 5, upper right plot).

**MAGNETIC
RESONANCE**
Discussions

Looking at $\Omega = \omega_I$ at X band, we see that the allowed EPR transition is almost completely saturated. Because the efficiency of the solid effect scales with $p = 1 - s$ (dashed orange arrow in fig. 2g) any gain from efficiently driving the forbidden transitions will be squashed down dramatically, thus substantially reducing the ultimate enhancement of the NMR signal. This observation implies that at X band the best solid-effect enhancement may occur at less than maximum mw power, as we

420 demonstrate numerically later.

The second row of fig. 5 shows the offset dependence of the transfer functions connecting the longitudinal component s_z^{ss} to the transverse components $s_{x,y}^{\text{ss}}$. The observed increase in magnitude from left to right reflects the multiplication by ω_1 of the functions $f_{x,y}$ which are independent of ω_1 (eq. (39)). These functions are the real (f_y) and imaginary (f_x) components of a complex-valued Lorentzian with width R_{2S} and center frequency $\Omega = 0$. In other words, they correspond to the absorptive and

425 dispersive components of a homogeneous EPR line. The absorptive component (blue line) is largest at $\Omega = 0$, while the two extrema of the dispersive component (orange line) are located at $\Omega = \pm R_{2S}$. At offsets much larger than the locations of these extrema (i.e., $\Omega \gg R_{2S}$), the absorptive component drops as $1/\Omega^2$ while the dispersive component drops as $1/\Omega$.

The third row of fig. 5 shows the net transfer functions relating the outputs of the Bloch equations, $s_{x,y}^{\text{ss}}$, to the input s_z^{eq}. They are obtained by multiplying the solid black lines in the first row with the lines in the second row. In essence, what we see

430 are the absorptive and dispersive components of a power-broadened EPR line. The power broadening (i.e., multiplication by $1 - s$) leads to qualitative differences. For example, while the peak of the blue line in the second row of the figure increased linearly with ω_1, it now decreases as $1/\omega_1$. In the case of the orange line, the locations of its extrema are now shifted towards larger offsets ($\Omega \approx \pm \omega_1 \sqrt{T_{1S}/T_{2S}}$) and their magnitude is approximately independent of B_1 ($\approx \sqrt{T_{2S}/T_{1S}}/2$, which equals $1/6 \approx 0.17$ for the choice of relaxation times in fig. 5). Clearly, the tail of the power-broadened dispersive (orange) component

435 extends further into the range of interest for the solid effect at high mw frequencies than the tail of the absorptive (blue) component. One could thus expect that s_x^{ss} contributes to the solid effect more than s_y^{ss}, simply because the latter does not survive at offsets equal to the nuclear Larmor frequencies at high fields. This observation is in line with the decision of Erb, Motchane and Uebersfeld to drop the therm proportional to s_y when arriving at (2) (Erb et al., 1958a).

The functions in the second row of fig. 5 were depicted as the even and odd components of the first filter in fig. 1. In fact,

440 we should have shown the power-broadened versions of these functions (third row of fig. 5). The peak of the solid blue line in fig. 1 would then be substantially reduced at high mw powers, providing additional reason for the absence of the solid effect in the vicinity of ω_S. In contrast, the peak of the dashed blue line is not reduced with power but only moves away from the EPR resonance position, without compromising the possibility of solid-effect DNP enhancement at the "wrong" offset which corresponds to the blue star in fig. 1.

445 ## 4.2 Steady state of the coupled Bloch equations

We now proceed to the analysis of the two coupled Bloch equations from fig. 3d. Our goal is to compare their steady state with fig. 3e and thus identify the forbidden-transition rates $v_\pm$. Because we already determined the electronic steady state, the problem we need to solve looks like shown in fig. 6a.
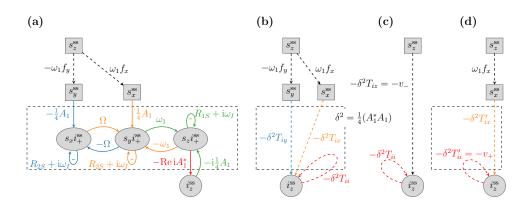
Figure 6. (**a**) Steady state of the generalized Bloch equations. (**b-d**) Transfer functions describing the steady-state relationship between the time derivative of i_z (output) and different choices of the electronic input.

In this figure, the outputs $s_{x,y}^{\mathrm{ss}}$ of the first set of Bloch equations serve as inputs to the second set of Bloch equations. This second set (enclosed in a dashed rectangle in fig. 6a) constitutes the dynamical system whose steady-state response we aim to characterize. In addition to the two inputs mentioned above, this system takes a third input (i_z) and produces the output that comes out of the red arrow. Our task is to determine the relationship between the three inputs and the output of this system at steady state.

The steady-state solution of (33) is

$$\begin{bmatrix} g_x^{\mathrm{ss}} \\ g_y^{\mathrm{ss}} \\ g_z^{\mathrm{ss}} \end{bmatrix} = -\mathrm{i}\frac{1}{4}A_1\mathscr{B}^{-1}\begin{bmatrix} -\mathrm{i}s_y^{\mathrm{ss}} \\ \mathrm{i}s_x^{\mathrm{ss}} \\ i_z^{\mathrm{ss}} \end{bmatrix}. \tag{41}$$

Because only g_z^{ss} feeds into the time derivative of i_z (eq. (29)), we have

$$\dot{i}_z|_{\mathrm{coh}}^{\mathrm{ss}} = -\delta^2\,\mathrm{Re}\Big\{\begin{bmatrix} 0 & 0 & 1 \end{bmatrix}\mathscr{B}^{-1}\begin{bmatrix} -\mathrm{i}s_y^{\mathrm{ss}} \\ \mathrm{i}s_x^{\mathrm{ss}} \\ i_z^{\mathrm{ss}} \end{bmatrix}\Big\}, \tag{42}$$

where the dipolar coupling was factored out as

$$\delta^2 = (A_1^*A_1)/4. \tag{43}$$

Clearly, the output is a linear combination of the three inputs and can be written as

$$\dot{i}_z|_{\mathrm{coh}}^{\mathrm{ss}} = -\delta^2(T_{ix}s_x^{\mathrm{ss}} + T_{iy}s_y^{\mathrm{ss}} + T_{ii}i_z^{\mathrm{ss}}), \tag{44}$$

which is illustrated in fig. 6b. Since δ has units of inverse time, the transfer functions T_{in} ($n = x, y, i$) must have units of time. Comparing (42) and (44), we see that

$$T_{iy} = \text{Re}\{-\mathrm{i}\mathscr{B}_{31}^{-1}\}, \quad T_{ix} = \text{Re}\{\mathrm{i}\mathscr{B}_{32}^{-1}\}$$
$$T_{ii} = \text{Re}\{\mathscr{B}_{33}^{-1}\}, \tag{45}$$

465   where $\mathscr{B}_{ij}^{-1}$ is the ijth element of the matrix $\mathscr{B}^{-1}$.

The needed matrix elements in the last *row* of $\mathscr{B}^{-1}$ can be obtained from the cofactors of the last *column* of $\mathscr{B}$ as follows:

$$\mathscr{B}_{31}^{-1} = \omega_1 \Omega / \Delta, \qquad \mathscr{B}_{32}^{-1} = \omega_1 (R_{2S} + \mathrm{i}\omega_I)/\Delta$$
$$\mathscr{B}_{33}^{-1} = [(R_{2S} + \mathrm{i}\omega_I)^2 + \Omega^2]/\Delta, \tag{46}$$

where the determinant of $\mathscr{B}$ is

$$\Delta = (R_{1S} + \mathrm{i}\omega_I)[(R_{2S} + \mathrm{i}\omega_I)^2 + \Omega^2] + \omega_1^2 (R_{2S} + \mathrm{i}\omega_I). \tag{47}$$

470   ### 4.2.1   Characterizing the second set of Bloch equations

Let us now introduce the complex-valued functions

$$F_y = \frac{1}{R_{2S} + \mathrm{i}\omega_I + \Omega \frac{1}{R_{2S} + \mathrm{i}\omega_I} \Omega}$$
$$F_x = \frac{\Omega}{R_{2S} + \mathrm{i}\omega_I} F_y, \quad H = \frac{1}{R_{1S} + \mathrm{i}\omega_I + \omega_1 F_y \omega_1}, \tag{48}$$

which generalize the functions (39) of the classical Bloch equations by supplementing their relaxation rates with an imaginary part. Like their classical analogs, these functions have units of time (Table 1). In terms of them, the matrix elements (46) can

475   be rewritten as

$$\mathscr{B}_{31}^{-1} = \omega_1 F_x H, \quad \mathscr{B}_{32}^{-1} = \omega_1 F_y H, \quad \mathscr{B}_{33}^{-1} = H. \tag{49}$$

Then, using (45), we express the three transfer functions of interest (fig. 6b) as

$$T_{ix,y} = \pm \omega_1 \text{Re}\{\mathrm{i}F_{y,x} H\}, \quad T_{ii} = \text{Re}\{H\}. \tag{50}$$

Because all steady-state properties of the second set of Bloch equations (inside the dashed rectangle in fig. 6a) are contained

480   in the functions (48), let us examine them more closely. These three complex-valued functions are plotted in the ω_I-Ω plane in fig. 7a. In these plots, the angular frequencies are reported in units of R_{2S}. Cross-sections at $\omega_I = 0, 0.5, 1.5, 3$ are drawn over the surfaces with solid black lines.

The black lines at $\omega_I = 0$ show that the imaginary parts of the functions F_y, F_x and H vanish and their real parts become equal to f_y, f_x and h of the classical Bloch equations (cf. fig. 5, first two rows). In particular, at $\omega_I = 0$, F_y and F_x as functions

485   of Ω are like the absorptive and dispersive components of the EPR line. To plot the function H we used $\omega_1 = 1.5$ (in units of
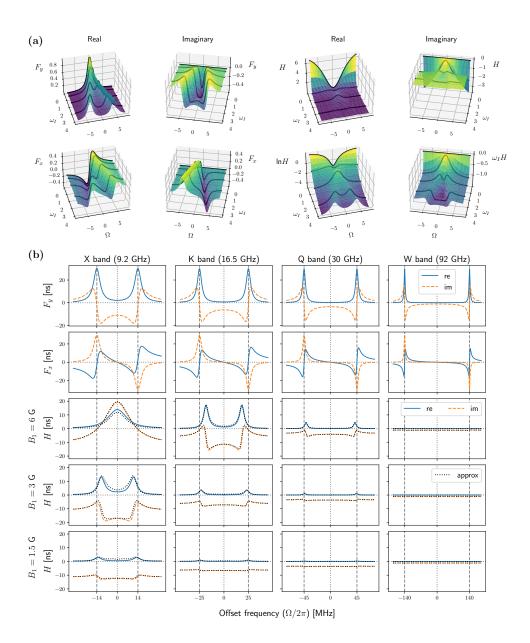
Figure 7. The functions F_y, F_x and H characterizing the steady state of the second set of Bloch equations. (**a**) Angular frequencies are measured in units of R_{2S}. $R_{1S} = R_{2S}/9$ as in the other figures. To calculate H we used $\omega_1 = 1.5$, which for $T_{2S} = 60$ ns corresponds to $B_1 \approx 1.5$ G. Solid black lines are cross-sections at $\omega_I = 0, 0.5, 1.5, 3$. (**b**) Numerical parameters as in fig. 5. Recall that $B_1 = 6$ G corresponds to $\omega_1/2\pi = 16.8$ MHz.

R_{2S}). Because both the real and imaginary parts of H decay very rapidly with increasing ω_I, we also show the logarithm of the real part and the product of the imaginary part with ω_I. These transformations make visible the small values at large ω_I.

MAGNETIC RESONANCE
Open Access Discussions

In fig. 7b we show these functions against Ω at four different nuclear Larmor frequencies and, in the case of H, three different mw powers. In each case, the locations of the Larmor frequencies along the horizontal axis are indicated with vertical dashed lines. In the first and second rows we see F_y and F_x, which do not change with mw power. The real and imaginary parts of F_y (first row) look like the real and imaginary parts of two complex-valued Lorentzians centered at $\Omega = -\omega_I$ and $\Omega = +\omega_I$. Indeed, with

$$L_\pm = [R_{2S} + i(\omega_I \pm \Omega)]^{-1}, \tag{51}$$

it is straightforward to show that $F_y = (L_- + L_+)/2$. These Lorentzians have the same width as f_y and f_x of the classical Bloch equations (fig. 5, second row). The function F_x in the second row of fig. 7b also has Lorentzian-like features centered at $\Omega = \pm\omega_I$, but the Lorentzian on the right is flipped around the horizontal axis. Indeed, it can be shown that $F_x = (L_- - L_+)/2$.

Differently from $F_{x,y}$, H depends on ω_1 (eq. (48)). In the last three rows of fig. 7b we plot $H(\Omega)$ for three different values of B_1, starting with $B_1 = 6\,\mathrm{G}$ (third row) and going down to $B_1 = 1.5\,\mathrm{G}$ (last row). The first thing to notice is that both the real (blue) and imaginary (orange) parts of this function decrease rapidly with increasing ω_I, i.e., moving to the right in a given row. (The former as $1/\omega_I^2$ and the latter as $1/\omega_I$.) As all transfer functions (50) are proportional to H, we expect these to also decrease rapidly with increasing nuclear Larmor frequency.

At the lower mw powers and higher magnetic fields H is seen to be dominated by its imaginary part, as its real part remains close to zero. At higher mw powers and lower magnetic fields ($B_1 = 6\,\mathrm{G}$, X and K bands, and $B_1 = 3\,\mathrm{G}$, X band) the real and imaginary parts are seen to be comparable in magnitude. Moving from the former to the latter regime, there is a major qualitative change: the features at $\Omega = \pm\omega_I$ shift towards the origin ($B_1 = 6\,\mathrm{G}$, K band, and $B_1 = 3\,\mathrm{G}$, X band) until they coalesce into a single line ($B_1 = 6\,\mathrm{G}$, X band).

In Paper II we calculate the inverse of the matrix $\mathscr{B}$ approximately using perturbation theory. The matrix element $\mathscr{B}_{33}^{-1} = H$ is found to be

$$H \approx \frac{\cos^2 \alpha}{\tilde{R}_1 + i\omega_I} + \frac{\frac{1}{2}\sin^2 \alpha}{\tilde{R}_2 + i(\omega_I - \omega_{\mathrm{eff}})} + \frac{\frac{1}{2}\sin^2 \alpha}{\tilde{R}_2 + i(\omega_I + \omega_{\mathrm{eff}})}, \tag{52}$$

where the frequency $\omega_{\mathrm{eff}} = \sqrt{\Omega^2 + \omega_1^2}$ corresponds to the effective magnetic field, α is the angle between this field and B_0 ($\cos\alpha = \Omega/\omega_{\mathrm{eff}}$, $\sin\alpha = \omega_1/\omega_{\mathrm{eff}}$), and

$$\tilde{R}_1 = R_{1S}(\cos\alpha)^2 + R_{2S}(\sin\alpha)^2$$
$$\tilde{R}_2 = R_{2S}[1 - (\sin\alpha)^2/2] + R_{1S}(\sin\alpha)^2/2. \tag{53}$$

This result is exact for $R_{1S} = R_{2S}$ and is perturbative in the difference of the two electronic relaxation rates.

The approximation (52) is shown with dotted black lines in the last three rows of fig. 7b. It is seen to correctly capture both the shift of the peaks towards smaller offsets and their coalescence at $\Omega = 0$. Inspecting (52) we see that the dependence of H on Ω is in the form of two Lorentzians centered at $\omega_{\mathrm{eff}} = \pm\omega_I$, which implies $\Omega^2 = \omega_I^2 - \omega_1^2$. This explains the deviation of the maxima from the canonical solid-effect positions $\Omega = \pm\omega_I$ for $\omega_1 \approx \omega_I$. At X band, when $B_1 = 6\,\mathrm{G}$, ω_1 is larger than ω_I and the two Lorentzians fuse together.
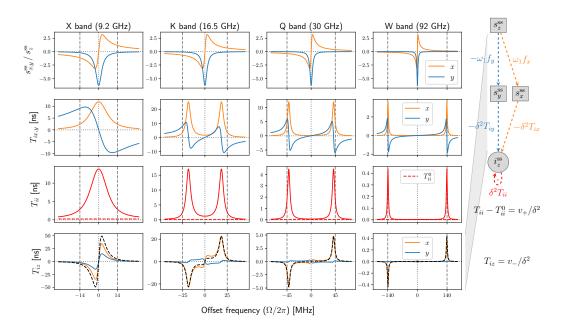
Figure 8. Transfer functions at the steady state of the coupled Bloch equations. $B_1 = 6\,\text{G}$, $T_{2S} = 60\,\text{ns}$ and $T_{1S} = 9\,T_{2S}$.

4.2.2 Combining the two sets of Bloch equations

Having examined the functions $F_{x,y}$ and H, we now turn to the transfer functions (50), which are indicated in fig. 6b. These are plotted in the second and third rows of fig. 8.

As T_{ii} (solid red lines) is just the real part of H, it exhibits all the features that we already talked about when discussing fig. 7b. Although, in principle, T_{ii} corresponds to the rate v_+, it accounts for both the two-step and four-step loops that we observed in fig. 3d. The former corresponds to the relaxation rate w_1 in fig. 2b, and is already included in R_{1I}. Hence its contribution has to be removed when identifying v_+.

Since the nuclear T_1 is typically measured with the microwaves switched off, we identify

$$T_{ii}^0 = \text{Re}\{H(\omega_1 = 0)\} = \text{Re}\{(R_{1S} + \text{i}\omega_1)^{-1}\} \tag{54}$$

as contributing to relaxation. Subtracting it from T_{ii}, we deduce

$$v_+/\delta^2 = T_{ii} - T_{ii}^0 = \text{Re}\{H - (R_{1S} + \text{i}\omega_1)^{-1}\}. \tag{55}$$

T_{ii}^0 is plotted with red dashed lines in the third row of fig. 8. At the high mw field that we have used ($B_1 = 6\,\text{G}$) it is negligible compared to T_{ii} itself (solid red line), thus subtracting the relaxation would not make much of a difference. However, at lower mw powers the contribution of T_{ii} to thermal relaxation becomes comparable to the rest, and the correction makes a difference. (This can be seen in the bottom plot of fig. 11 where $B_1 = 1\,\text{G}$.)

MAGNETIC
RESONANCE
Discussions
Open Access

In the second row of fig. 8, the functions $T_{ix,y}$ resulted from the product of $F_{y,x}$ and H (eq. (50)). Interestingly, their
Lorentzian-like features are at the same frequency offsets as those of T_{ii}, the real part of H. (The functions $T_{ix,y}$ were shown
in fig. 1 as the even and odd components of the second filter). We observe that T_{ix} (orange) and T_{iy} (blue) are similar in
magnitude. Thus, if the inputs s_x^{ss} and s_y^{ss} were comparable in magnitude, the contributions of the two parallel branches from
s_z^{ss} to the output would be similar (see flow diagram in the right margin of fig. 8). We know, however, that s_y^{ss} is much smaller
than s_x^{ss} at large offsets, and so the path via T_{ix} (orange) will contribute more.

To determine the rate v_-, which connects s_z to the time derivative of i_z at steady state (fig. 6c), we should treat s_z^{ss} as an
input (not $s_{x,y}^{\text{ss}}$). Multiplying the functions $T_{ix,y}$ (fig. 8, second row) by the functions in the first row, we obtain the orange and
blue lines in the last row of the figure. (The functions in the first row were shown before in fig. 5. They are plotted here again
only for $B_1 = 6\,\text{G}$. The four plots are identical to each other but appear different due to the different scales of the horizontal
axes.) Comparing the first and second rows of fig. 8, we see that an odd/even function in the first row is multiplied by an
even/odd function in the second row to produce the corresponding orange and blue lines in the bottom row. As a result, the
contribution of both parallel paths from s_z^{ss} to i_z^{ss} (via either s_x^{ss} or s_y^{ss}) is odd in Ω.

The cumulative transfer function of the two parallel paths is obtained by adding the orange and blue lines in the last row of
fig. 8. It equals (compare fig. 6b and fig. 6c)

$$T_{iz} = \omega_1 f_x T_{ix} - \omega_1 f_y T_{iy} = v_-/\delta^2, \tag{56}$$

and is also plotted in the last row of fig. 8 with black dashed lines.

As already mentioned in the introduction, this cumulative transfer function results from two band-pass filters connected in
series and centered at $\Omega = 0$ (fig. 8, top row) and at $\Omega \approx \pm\omega_I$ (fig. 8, second row). The composite filter (fig. 8, bottom row)
will only "pass a signal" to the extend that the tails of the "dispersive" component of one of the filters and the "absorptive"
component of the other filter overlap. When this overlap is small, the corresponding transitions are "forbidden".

At Q and W bands the cumulative transfer function (fig. 8, bottom row, black dashed lines) is seen to be essentially iden-
tical to its first additive contribution $\omega_1 f_x T_{ix}$ (orange line), which means that the electronic polarization is transferred to the
nucleus almost entirely through the dispersive component s_x^{ss}. This conclusion supports the assumption of Erb, Motchane and
Uebersfeld (Erb et al., 1958a).

From (56) and (50) we have

$$T_{iz} = \omega_1^2 \, \text{Re}\{i(f_x F_y + f_y F_x)H\}. \tag{57}$$

Incidentally,

$$f_x F_y + f_y F_x = f_x F_y \frac{2R_{2S} + i\omega_I}{R_{2S} + i\omega_I} = f_x F_y', \tag{58}$$

where the last equality defines F_y'. The second R_{2S} in the numerator of (58) comes from $f_y F_x$ and can be viewed as a
"correction" to $f_x F_y$ due to $f_y F_x$. The last row of fig. 8 already demonstrated that this correction becomes negligible at
increasingly large nuclear Larmor frequencies. Here we see this analytically.

Using (58) the cumulative transfer function from s_z^{ss} to i_z^{ss} can be expressed as if there was only one path through s_x^{ss}, as illustrated in fig. 6d. In other words, it is possible to rewrite (44) exactly, in a way that contains s_x^{ss} but does not contain s_y^{ss}:

$$\dot{i}_z|_{\mathrm{coh}}^{\mathrm{ss}} = -\delta^2(T_{ix}' s_x^{\mathrm{ss}} + T_{ii} i_z^{\mathrm{ss}}), \tag{59}$$

with

570 $$T_{ix}' = \omega_1 \mathrm{Re}\{\mathrm{i} F_y' H\}. \tag{60}$$

(Compare this T_{ix}' with T_{ix} in eq. (50).) Hence, the phenomenological equation (2) of Erb, Motchane and Uebersfeld is, in fact, exact with $\nu = -\delta^2 T_{ix}'$.

In summary, we derived the following exact expressions for the rate constants of the forbidden transitions:

$$v_+ = \delta^2(T_{ii} - T_{ii}^0), \quad v_- = \delta^2 T_{iz} = \delta^2(\omega_1 f_x) T_{ix}'. \tag{61}$$

575 ## 5 Use of the rate constants

5.1 Relation to the classical rates

Now we show that the classical expression (5) follows from the exact rates when $\omega_1 \ll \omega_I$.

To simplify the analysis, we take from the start a long electronic T_1 relaxation time, such that $R_{1S} \ll \omega_I$. This should be the case under solid-effect DNP conditions where the electronic T_1 is at least a microsecond. In this case the function H (eq. (48))

580 simplifies to

$$H \approx \frac{1}{\mathrm{i}\omega_I + \omega_1^2 F_y} = \frac{1}{\mathrm{i}\omega_I}\left(1 + \frac{\omega_1^2}{\mathrm{i}\omega_I} F_y\right)^{-1}. \tag{62}$$

For $\omega_1 \ll \omega_I$, to first order in ω_1^2,

$$H \approx \frac{1}{\mathrm{i}\omega_I} + \frac{\omega_1^2}{\omega_I^2} F_y. \tag{63}$$

From (61), retaining only terms of up to first order in ω_1^2,

585 $$v_+ \approx \delta^2 \frac{\omega_1^2}{\omega_I^2}\mathrm{Re}\{F_y\}, \quad v_- \approx \delta^2 \frac{\omega_1^2}{\omega_I^2}\omega_I f_x \mathrm{Re}\{F_y'\}. \tag{64}$$

To establish the equivalence of these expressions with (5), we need to show that $\mathrm{Re}\{F_y\}$ and $\omega_I f_x \mathrm{Re}\{F_y'\}$ equal, respectively, the sum and difference of two real-valued Lorentzians centered at $\Omega = \pm\omega_I$. For the complex-valued Lorentzians (51), we already observed that $L_- + L_+ = 2F_y$. One can also confirm that $\mathrm{Re}\{L_- - L_+\} = 2\omega_I f_x \mathrm{Re}\{F_y'\}$. Hence,

$$v_\pm \approx \frac{1}{2}\delta^2 \frac{\omega_1^2}{\omega_I^2}(\mathrm{Re}\{L_-\} \pm \mathrm{Re}\{L_+\}), \tag{65}$$
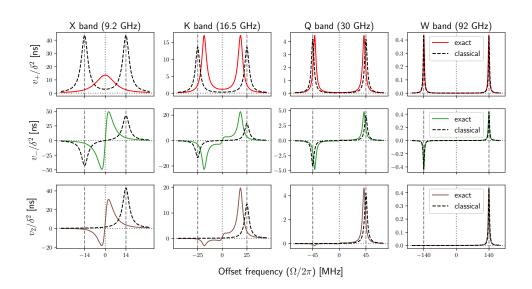
Figure 9. Forbidden-transition rates calculated either exactly (solid lines) or using the classical expression (5) with $v_\pm = v_2 \pm v_0$ (dashed lines). As in the previous figures, $B_1 = 6\,\text{G}$, $T_{2S} = 60\,\text{ns}$ and $T_{1S} = 9\,T_{2S}$.

and thus

$$v_{0,2} \approx \frac{1}{8}(A_1^* A_1)\left(\frac{\omega_1}{\omega_I}\right)^2 \text{Re}\{L_\pm\}, \tag{66}$$

which is the classical result (5).

The sum and difference of the classical rates v_2 and v_0 is compared with the exact $v_\pm$ in the first two rows of fig. 9. Naturally, the Lorentzians associated with the classical rates remain centered at $\pm\omega_I$ even when the maxima of the exact rates shift closer to each other at Q and K bands, and converge at X band. At high fields (e.g. W band), where $\omega_I \gg \omega_1$, the classical approximations work perfectly.

In the last row of fig. 9 we show the DQ-transition rate v_2. While, classically, it is always non-negative (black dashed lines), the exact rate deduced from $v_\pm$ (solid brown lines) is seen to become negative at some offsets. From the perspective of the rate-equation formalism, such negative rates are meaningless. In that sense, the description of the forbidden transitions in terms of $v_\pm$ is more fundamental than their description in terms of v_0 and v_2.

5.2 Solid-effect DNP enhancement

The DNP enhancement of the solid effect (eq. (22)) was the product of $|\gamma_S|/\gamma_I$ with the following two factors:

$$p_X = \frac{R_{1I}/\delta^2}{R_{1I}/\delta^2 + (T_{ii} - T_{ii}^0)}, \qquad \frac{pv_-}{R_{1I}} = \frac{pT_{iz}}{R_{1I}/\delta^2}, \tag{67}$$

which we have rewritten here in terms of the transfer functions T_{ii}, T_{ii}^0 and T_{iz}. These transfer functions already appeared in the last two rows of fig. 8. Thus, to calculate the DNP enhancement, we only need to specify the ratio R_{1I}/δ^2.

In the case of δ, rather than calculating A_1 (eq. (28)) for some arbitrary inter-spin vector, let us average $A_1^* A_1$ over the entire 3D space. With b denoting the so called "distance of closest approach" or "contact distance", and N denoting the number of electron spins per unit volume, we have

$$\langle \delta^2 \rangle = \frac{1}{4} \langle A_1^* A_1 \rangle = D_{\text{dip}}^2 \frac{6\pi}{5} \frac{N}{3b^3}, \qquad (68)$$

610 where, in this case, the angular brackets denote spatial averaging. We will use $b = 1\,\text{nm}$ and $N = 0.1\,\text{M}$ as representative, but otherwise arbitrary values.

While the average over 3D space in (68) is clear mathematically, it is important to understand that physically it implies fast spin diffusion (Wind et al., 1985). Since the nuclear polarization in solids is homogenized across the sample through spin diffusion, replacing the individual δ^2's of the nuclear spins by the average over all nuclei is only legitimate when spin diffusion

615 is faster than the nuclear spin-lattice relaxation. In practice, spin diffusion is rather slow and is often the bottleneck for efficient polarization transfer in solids (Hovav et al., 2011; Smith et al., 2012; Pinon, 2018). As a result, the DNP enhancement values that we will calculate with (68) are expected to be appreciably larger than what could be observed experimentally.

Similar considerations also apply for the choice of the nuclear spin-lattice relaxation time. In principle T_{1I} will depend on the distance of the nucleus from the electronic spin, and thus will vary greatly across the sample. In the limit of fast spin

620 diffusion, however, only its average value becomes relevant. In general, this time depends on the radical concentration and on the magnetic field B_0. However, for the purposes of illustration, here we take a generic numerical value of $T_{1I} = 30\,\text{ms}$ across all mw bands. Again, this value is realistic but otherwise arbitrary.

Using $b = 1\,\text{nm}$, $N = 0.1\,\text{M}$ and $T_{1I} = 30\,\text{ms}$ we find $R_{1I}/\langle \delta^2 \rangle = 1.78\,\text{ns}$. Let us visually compare this time scale with $(T_{ii} - T_{ii}^0) = v_+ / \langle \delta^2 \rangle$ by consulting the solid red line in the first row of fig. 9. We observe that at X and K bands the maxima

625 of the red line are much larger than 2 ns, which means that the minima of p_X will be close to zero. At Q band the maxima of the red line are comparable to 2 ns, and at W band they are much smaller. The minima of the nuclear cross-polarization factor are thus expected to be about one half and one, respectively. These expectations are confirmed by the maroon lines in the first row of fig. 10, which demonstrate that p_X can substantially deviate from one at lower magnetic fields.

To estimate the expected magnitude of the second factor in (67), we need to compare the time scale $R_{1I}/\langle \delta^2 \rangle = 1.78\,\text{ns}$ with

630 pT_{iz}. While T_{iz} was shown with black dashed lines in the bottom row of fig. 8, now it has to be multiplied by the electronic polarization factor in the top row of fig. 5. From the line for $B_1 = 6\,\text{G}$ in this row, we see that T_{iz} will be significantly suppressed at X band, so it is hard to judge how the reduced value will compare with 1.78 ns. At Q band, T_{iz} will be reduced by a little more than a factor of two, which will make its peak in fig. 8 comparable to $R_{1I}/\langle \delta^2 \rangle$. At W band, where the factor p is about 0.9, T_{iz} will be only slightly reduced, so its peak is expected to be about one fifth of 1.78 ns. Again, these estimates

635 are confirmed by the green lines in the second row of fig. 10.

The last row of fig. 10 shows the product of the first two rows times $|\gamma_S|/\gamma_I$, assuming a proton spin. The result is the solid-effect DNP enhancement (eq. (22)). In the figure we have also shown the factors predicted by the classical expression of the rates (eq. (5)) with black dashed lines. While there are quantitative differences between the exact calculations and the classical approximation, the magnitudes of the DNP enhancements in the two cases are, in fact, comparable. A closer look
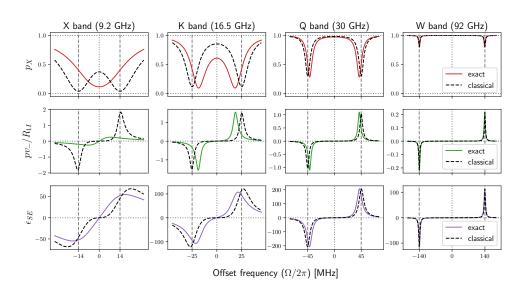
Figure 10. Decomposition of the DNP field profile (ϵ_{SE}) in terms of the multiplicative contributions p_X and pv_-/R_{1I}. The new parameters used here are $T_{1I} = 30\,\mathrm{ms}$, $b = 1\,\mathrm{nm}$ and $N = 0.1\,\mathrm{M}$. Other parameters: $B_1 = 6\,\mathrm{G}$, $T_{2S} = 60\,\mathrm{ns}$ and $T_{1S} = 9\,T_{2S}$.

reveals that, for the specific B_1 and relaxation times used in the calculations, the classical description of the solid effect (eq. (5)) works perfectly at Q band and at larger mw frequencies. (In fig. 12 we show that by reducing the mw power to $B_1 = 1\,\mathrm{G}$ the classical expressions are also perfect at X band.) The amplitudes of the maximum enhancements at the four mw bands are roughly in the ratios $1:2:4:2$ (X:K:Q:W). On the other hand, considering the inverse dependence on ω_I^2, we expect the ratios $100:40:10:1$. These expected ratios are indeed observed at the much lower mw power of $B_1 = 1\,\mathrm{G}$ (fig. 12, lower plot). Comparison of figs. 10 and 12, shows that increasing B_1 increases the amplitudes of the maximum enhancements at W and Q bands, but reduces the enhancement at X band. Such reduction of the solid-effect DNP enhancement with increasing B_1 has been reported at X band (Neudert et al., 2016).

6 Conclusion

In this paper we presented a way of thinking about the solid effect which was grounded in the dynamics of the spins at steady state. The spin dynamics of the four-level system that we analyzed requires only 16 different spin operators, including the identity operator. It is thus completely described by a 16×16 propagation matrix in Liouville space, and can be simulated numerically using a spin-dynamics simulation package (Bengs and Levitt, 2018; Yang et al., 2022). Such numerical simulations would provide answers to many specific questions, including the efficiency of the solid effect for the parameters that we explored here. Nevertheless, having an intuitive understanding of the spin dynamics which is relevant for a given phenomenon is invaluable.

MAGNETIC RESONANCE
Open Access Discussions

Here, we followed a systematic procedure for deriving the relevant equations of motion under a given spin Hamiltonian (Sec. 3.2), and developed a graphical representation to visualize the interplay of these equations (fig. 3d). While our analysis focused on the solid effect and the Hamiltonian (27), it should be possible to analyze other related effects with different Hamiltonians in a similar way. In any case, for a four-level system the resulting dynamics will comprise at most fifteen coupled differential

660 equations. Here, we explicitly considered the dynamics of seven spin operators (fig. 3d), while the dynamics of three more operators, namely $S_n I_-$ ($n = x, y, z$), was included implicitly when we took the real part of $s_z i_+$. The remaining five operators which did not appear in our analysis were $I_\pm$ and $S_n I_z$.

The main insight of our dynamical description of the solid effect relates to the role of the coherences. We demonstrated the involvement of two types of coherences: purely electronic and mixed electron-nuclear. Their evolution was described by two

665 coupled Bloch equations (fig. 3d), whose steady-state response was rationalized in terms of two band-pass filters connected in series (figs. 8 and 1). The involvement of the electron-nuclear coherences in the solid effect is directly manifested by the lines in the DNP field profile at the canonical offsets $\Omega \approx \pm\omega_I$. The involvement of the purely electronic coherences, on the other hand, is not directly visible, at least until one recognizes that the odd parity of the DNP field profile is a manifestation of the dispersive EPR line, as intuited by Erb, Motchane and Uebersfeld (Erb et al., 1958a).

670 On a more quantitative level, we predicted that when the mw nutation frequency becomes comparable to the nuclear Larmor frequency, the optimal excitation of the forbidden transitions should shift from the canonical solid effect positions to smaller offsets (fig. 9). Considering the high mw powers accessible in modern-day DNP spectrometers (Neudert et al., 2016), this observation should be relevant at S and X bands (Neudert et al., 2017; Gizatullin et al., 2021). However, because of the additional multiplication by the electronic polarization factor (fig. 5, top row), the maxima of the enhancement end up in the

675 vicinity of the canonical offsets even when the condition $\omega_1 \ll \omega_I$ is violated (fig. 10, last row, X band).

The classical explanation of the solid effect in terms of level mixing (Abragam and Proctor, 1958) is static in nature and is thus hard to generalize to liquids where the dipolar interaction fluctuates randomly due to molecular motions. The time-dependent description of the solid effect that we developed in the current paper naturally accommodates such stochastic modulation of the parameters of the Hamiltonian, in a way similar to the treatment of relaxation in liquids (Abragam, 1961). In

680 the companion paper we extend the formalism to the solid effect in liquids, and validate its predictions against recent DNP experiments at J band (Kuzhelev et al., 2022).
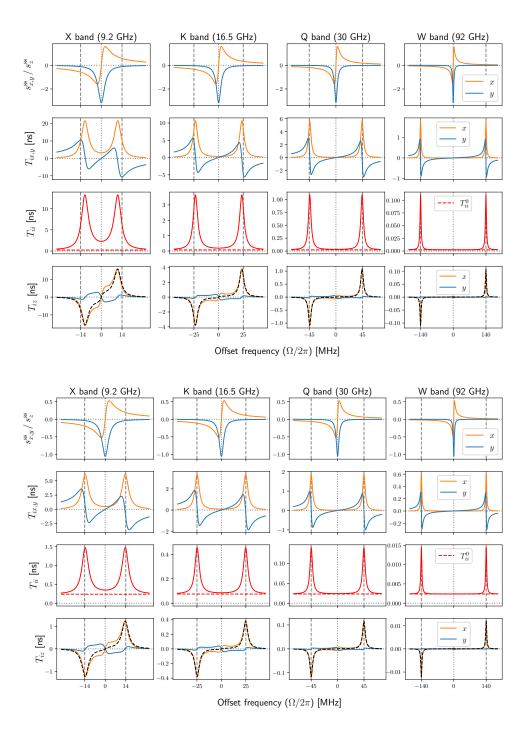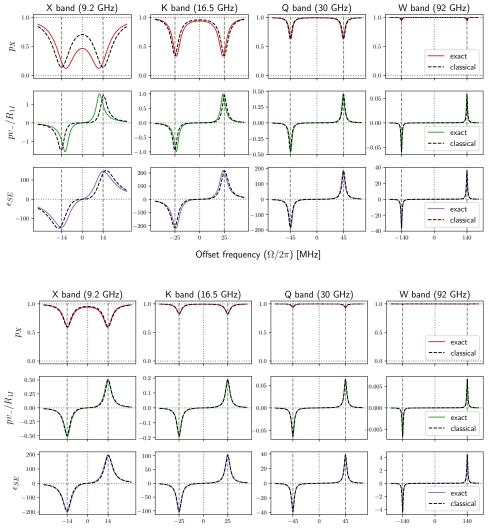
Figure 11. Same as fig. 8 with smaller mw fields of $B_1 = 3\,\text{G}$ (top) and $B_1 = 1\,\text{G}$ (bottom).

Figure 12. Same as fig. 10 with smaller mw fields of $B_1 = 3\,\text{G}$ (top) and $B_1 = 1\,\text{G}$ (bottom).

685

MAGNETIC RESONANCE
Open Access Discussions

References

Abragam, A.: Overhauser Effect in Nonmetals, Physical Review, 98, 1729–1735, https://doi.org/10.1103/PhysRev.98.1729, 1955.

Abragam, A.: The Principles of Nuclear Magnetism, Oxford University Press, New York, 1961.

690 Abragam, A. and Proctor, W. G.: Une nouvelle méthode de polarisation dynamique des noyaux atomiques dans les solides, Compt. rend., 246, 2253–2256, 1958.

Barker, W. A.: Dynamic Nuclear Polarization, Reviews of Modern Physics, 34, 173–185, https://doi.org/10.1103/RevModPhys.34.173, 1962.

Bengs, C. and Levitt, M. H.: SpinDynamica: Symbolic and numerical magnetic resonance in a Mathematica environment, Magnetic Resonance in Chemistry, 56, 374–414, https://doi.org/https://doi.org/10.1002/mrc.4642, 2018.

695 Erb, E., Motchane, J.-L., and Uebersfeld, J.: Effet de polarisation nucléaire dans les liquides et les gaz adsorbés sur les charbons, Compt. rend., 246, 2121–2123, 1958a.

Erb, E., Motchane, J.-L., and Uebersfeld, J.: Sur une nouvelle méthode de polarisation nucléaire dans les fluides adsorbés sur les charbons. extension aux solides et en particulier aux substances organiques irradiées., Compt. rend., 246, 3050–3052, 1958b.

Gizatullin, B., Mattea, C., and Stapf, S.: Molecular Dynamics in Ionic Liquid/Radical Systems, The Journal of Physical Chemistry B, 125, 4850–4862, https://doi.org/10.1021/acs.jpcb.1c02118, 2021.

700

Gizatullin, B., Mattea, C., and Stapf, S.: Three mechanisms of room temperature dynamic nuclear polarization occur simultaneously in an ionic liquid, Physical Chemistry Chemical Physics, 24, 27 004–27 008, https://doi.org/10.1039/D2CP03437A, 2022.

Hovav, Y., Feintuch, A., and Vega, S.: Dynamic nuclear polarization assisted spin diffusion for the solid effect case, The Journal of Chemical Physics, 134, 074 509, https://doi.org/10.1063/1.3526486, 2011.

705 Kuzhelev, A. A., Dai, D., Denysenkov, V., and Prisner, T. F.: Solid-like Dynamic Nuclear Polarization Observed in the Fluid Phase of Lipid Bilayers at 9.4 T, Journal of the American Chemical Society, 144, 1164–1168, https://doi.org/10.1021/jacs.1c12837, 2022.

Leblond, J., Uebersfeld, J., and Korringa, J.: Study of the Liquid-State Dynamics by Means of Magnetic Resonance and Dynamic Polarization, Physical Review A, 4, 1532–1539, https://doi.org/10.1103/PhysRevA.4.1532, 1971.

Neudert, O., Mattea, C., and Stapf, S.: A compact X-Band resonator for DNP-enhanced Fast-Field-Cycling NMR, Journal of Magnetic Resonance, 271, 7–14, https://doi.org/https://doi.org/10.1016/j.jmr.2016.08.002, 2016.

710

Neudert, O., Mattea, C., and Stapf, S.: Molecular dynamics-based selectivity for Fast-Field-Cycling relaxometry by Overhauser and solid effect dynamic nuclear polarization, Journal of Magnetic Resonance, 276, 113–121, https://doi.org/https://doi.org/10.1016/j.jmr.2017.01.013, 2017.

Pinon, A. C.: Spin Diffusion in Dynamic Nuclear Polarization Nuclear Magnetic Resonance, Ph.D. thesis, EPFL, 2018.

715 Smith, A. A., Corzilius, B., Barnes, A. B., Maly, T., and Griffin, R. G.: Solid effect dynamic nuclear polarization and polarization pathways, The Journal of Chemical Physics, 136, 015 101, https://doi.org/10.1063/1.3670019, 2012.

Solomon, I.: Relaxation Processes in a System of Two Spins, Phys. Rev., 99, 559–565, 1955.

Van Kampen, N. G.: Elimination of fast variables, Physics Reports, 124, 69–160, https://doi.org/https://doi.org/10.1016/0370-1573(85)90002-X, 1985.

720 Webb, R. H.: Steady-State Nuclear Polarizations via Electronic Transitions, American Journal of Physics, 29, 428–444, https://doi.org/10.1119/1.1986008, 1961.

Wenckebach, T.: Essentials of Dynamic Nuclear Polarization, Spindrift Publications, The Netherlands, 2016.

Wind, R. A., Duijvestijn, M. J., van der Lugt, C., Manenschijn, A., and Vriend, J.: Applications of dynamic nuclear polarization in 13C NMR in solids, Progress in Nuclear Magnetic Resonance Spectroscopy, 17, 33–67, https://doi.org/https://doi.org/10.1016/0079-6565(85)80005-4, 1985.

725

Yang, C., Ooi Tan, K., and Griffin, R. G.: DNPSOUP: A simulation software package for dynamic nuclear polarization, Journal of Magnetic Resonance, 334, 107 107, https://doi.org/https://doi.org/10.1016/j.jmr.2021.107107, 2022.